ELSEVIER

Journal of Nuclear Materials 306 (2002) 61–72

journal of nuclear materials

www.elsevier.com/locate/jnucmat

Molecular dynamics simulation of the α-recoil nucleus displacement cascade in zirconolite

L. Veiller [a], J.-P. Crocombette [a,*], D. Ghaleb [b]

[a] *Commissariat à l'Énergie Atomique, Service de Recherches de Métallurgie Physique, CEA/DEN-DMN-SRMP, CE Saclay, Gif sur Yvette cedex, 91191 France*

[b] *Commissariat à l'Énergie Atomique, CEA/DEN-DIEC-SESC-LCLT, Marcoule, France*

Received 26 April 2002; accepted 23 July 2002

Abstract

Molecular dynamics simulation with Buckingham empirical potentials has been used to study irradiation damage in crystalline zirconolite ($CaZrTi_2O_7$). Threshold displacement energies have been calculated and displacement cascades (DCs) initiated by α-decay recoil nuclei have been modeled. DCs result in an highly disordered core around the track of the projectile surrounded by a distribution of isolated point defects. The number and types of point defects created by the cascades are calculated. Radial distribution functions of ions in the disordered core are intermediate between the ones of crystalline and amorphous zirconolite. The simulated cascades are consistent with the experimentally observed direct impact amorphization associated with phase transitions in the crystalline areas.

1. Introduction

Nowadays, strategies are being developed for the immobilization of actinide-rich waste from the reprocessing of spent fuel from commercial reactors and subsequent partitioning of the high-level radioactive waste (HLW). Waste forms currently under consideration for permanent deposition of HLW include glasses and ceramic hosts. In France, legislation has favored intensive research on enhanced separation and conditioning or transmutation of long-lived radionuclides from HLW. Current research on advanced chemical separation processes for the long-lived actinides and the possible option of geological disposal if transmutation is not adopted, have prompted investigation of new confinement matrices, such as ceramics, as potential ultimate host materials.

Zirconolite ($CaZrTi_2O_7$) is among the actinide-bearing phases which has been proposed as a crystalline confinement matrix for the long-term disposal of actinides (Cm, Am, Pu, ...) issued from HLW (e.g. France) and from excess weapons-grade plutonium (e.g. USA). The zirconolite host mineral has successfully demonstrated its ability to retain considerable quantities of naturally occurring radioactive elements (e.g. U, Th), in a variety of environments over geological time [1,2]. Trivalent and tetravalent actinides readily substitute for calcium and zirconium sites respectively [3]. At low concentrations, substitutions simply result in a solid solution. As a result of the α-decay process, the α-recoil nuclei collide mainly elastically with the surrounding atoms and localized displacement cascades (DCs) occur in the material. This is the main source of defect production and modifications of the crystalline structure in HLW host materials subjected to α-decay irradiation in repository areas. Under such irradiation, zirconolite undergoes a crystalline to amorphous transformation with has an associated volume expansion. These phenomena have been extensively studied (see the reviews

---

[*] Corresponding author. Tel.: +33-1 69 08 92 85; fax: +33-1 69 08 68 67.

E-mail address: jpcrocombette@cea.fr (J.-P. Crocombette).

0022-3115/02/$ - see front matter © 2002 Elsevier Science B.V. All rights reserved.
PII: S0022-3115(02)01134-0

by Weber et al. [4] and Ewing et al. [5]). Even if the radiation effects on the stability and durability of the waste forms have been actively pursued, there is a lack of basic understanding on the radiation-damage process. The subsequent evolution of the primary damage over geological time scales ($> 10^5$ years), can give rise to important changes in the microstructure and strongly affect the containment properties of the matrix. Models of such a long-term behavior require at their starting point an accurate description of the defect state resulting from the cascade displacements. The processes associated with a DC occur over length and time scales (i.e. nm and ps) that are difficult to study experimentally but constitute ideal subjects for atomic-scale computer simulation studies [6–9]. The aim of the present paper is to model, at the atomic level, the effects of DCs initiated by elastic loses of the α-recoil nuclei by means of molecular dynamics (MD) simulation. For that purpose, we have established a set of two-body potentials of the Buckingham type for zirconolite.

The set of the potential parameters fitted to the zirconolite structural equilibrium properties is presented. Using the established force field, we have first calculated the threshold displacement energies (E_d) of the various kinds of atoms by means of MD. Then a few displacements cascades have been simulated with kinetic energies up to 12 keV, the main result being that a cascade produces an highly disordered track surrounded by a distribution of isolated point defects.

2. Methodology

2.1. Technicalities

A very accurate description of mineral structures can be obtained using empirical potentials. The best empirical potentials include the ion polarization effects, for instance by using a shell model [10] in which the electronic cloud is linked to the core ion by a spring of constant stiffness. But DCs cannot be modeled with such a kind of potentials. Indeed, under ballistic collisions, some ion cores experience a very fast increase of their kinetic energies. As electron shells do not experience such collisions, an artificial and unrealistic separation appears between the ion cores and their electron shell. Hence, only empirical potentials of the rigid-ion model type can be used. Our model of $\mathrm{CaZrTi_2O_7}$ is fully ionic and consists of $\mathrm{Ca^{2+}}$, $\mathrm{Zr^{4+}}$, $\mathrm{Ti^{4+}}$ and $\mathrm{O^{2-}}$ ions and we used the Buckingham potential form to express the two-body short-range interactions [11,12]. The interaction energy between ion types i and j can be expressed as follows:

$$U_{ij}(r_{ij}) = A_{ij}\exp\left(\frac{-r_{ij}}{\rho_{ij}}\right) - \frac{C_{ij}}{r_{ij}^6} + \frac{1}{4\pi\varepsilon_0}\frac{Z_iZ_je^2}{r_{ij}}\mathrm{erfc}\left(\frac{r_{ij}}{\eta}\right), \tag{1}$$

where r_{ij} is the interionic distance, Z_ie and Z_je are the formal charges of the ions and A_{ij}, ρ_{ij} and C_{ij} are adjustable parameters to be determined and $\eta = 6.7$ Å. The first two terms correspond to the short-range (Buckingham) potentials and represent both the repulsive interactions due to overlap of the ions (Born–Mayer exponential term of Eq. (1)) and the attractive van der Waals interaction between them (inverse sixth-power function of Eq. (1)). The last term of Eq. (1) can be viewed as a screened Coulombic term. The complementary error function acts on the ionic charges Z_ie and Z_je reducing them to lower values as a function of the interaction distance r_{ij}. This expression of Coulomb energy comes from a restriction to the real part of an Ewald summation method [13]. We truncated the potentials at a cutoff radius of 11.2 Å. Neglecting the so-called reciprocal space term of the Ewald summation (thus reducing the range of Coulombic interactions) is a common approximation in empirical potentials simulations of oxides. It has recently been proved that this approximation has barely no effect on the structure of complex oxide glasses [14]. What for concerns DCs, MD simulations on nuclear glasses with the complete Ewald summation evidenced small displacements of mobile alkaline ions in the periphery of DCs due to long range electrical field effects [14,15]. Our form of the potential cannot reproduce such effects but they are not expected to appear in crystalline zirconolite. For interatomic distances smaller than 0.9 Å, the pair potential is of the Ziegler–Biersack–Littmark type [16]. The two kinds of potentials are connected (between 0.9 and 1.0 Å) with a fifth order polynomial to ensure continuity of the potential and of its two first derivatives.

Except when otherwise stated, the MD simulations were performed in the microcanonical ensemble that is under conditions of constant particle number, volume and energy (NVE). We performed the calculations with a parallel version of the code that was formerly used to simulate cascades in zircon [9], nuclear glasses [8] and metals [7]. The ionic trajectories of the atoms are obtained by integrating Newton's equations of motion, using the Verlet algorithm [17]. The forces are derived from the interatomic potential energy (Eq. (1)) between the atoms in the system.

2.2. Force field for zirconolite

To establish the parameters entering Eq. (1), we used the program GULP (general utility lattice program) which implements an algorithm for equilibrating the crystal structure [11]. In this program, the parameters of the potential are empirically derived by a least-squares fitting routine, so as to achieve the best possible agreement between calculated and experimental crystal properties. Unfortunately, in the case of zirconolite, very few experimental figures are at our disposal to fit the potentials. Thus the fit was made on the experimental values of the lattice parameters and of the atomic positions only (see below). After determination of the parameters, the variation with temperature of the specific heat and the calculated density have been compared with experimental data in order to validate the established potentials; details can be found elsewhere in a previous paper [18].

We considered the structure of zirconolite described by Rossell [19]. Zirconolite, nominally $CaZrTi_2O_7$ ($Z = 8$), has a monoclinic structure and belongs to the centrosymmetric C2/c space group (no. 15, C^6_{2h}). The three different cations (Ca, Zr, Ti) are ordered onto five different sites with three sites for titanium: two six-coordinated sites (Ti(1), Ti(3)) and one five-coordinated site (Ti(2)). The crystal structure of zirconolite is best described as a layer structure in which layers of Ti polyhedra lie parallel to (0 0 1) planes and alternate with planes containing Ca and Zr. The distorted TiO_6 octahedra are arranged in three-membered and six-membered rings to form continuous 2D-sheets. These (0 0 1) sheets are interleaved by planes containing Ca and Zr atoms ordered into alternating [1 1 0]-type rows as shown in Fig. 1. The calcium atoms are located in distorted cubic polyhedra, while the zirconium atoms are seven fold oxygen coordinated in face-capped octahedra. Situated within the six-membered TiO_6 rings are pairs of statistically occupied TiO_5 trigonal bipyramids.

As formal charges were considered, the fit was restricted to the A_{ij}, ρ_{ij} and C_{ij} parameters. Some restrictions were imposed on the parameter variations in order to ensure a better convergence of the fitting routine: the cation–cation interactions other than Coulombic ones, were set to zero, as well as the C_{ij} parameters of the cation–oxygen interactions. For oxygen–oxygen interactions we kept the original values of the exponential Born–Mayer repulsion coefficients for O^{2-}–O^{2-} interaction published by Catlow [20], the fit being restricted to the C_{ij} parameter.

The fitted parameters of the short-range potentials are given in Table 1 while the calculated properties compared to the experimental ones are given in Table 2. One can see that the characteristics of the cell parameters of monoclinic zirconolite are reproduced within 4% by our force field which is quite satisfactory. As far as we know, there is no published experimental value for the bulk modulus for zirconolite. However, our computed value (224.3 GPa) is quite in agreement with experimental values measured for other crystalline oxides ceramics (e.g. 225.2 GPa for zircon $ZrSiO_4$ [21] and around 210 GPa for Y_2O_3-stabilized zirconia ZrO_2 [22]).

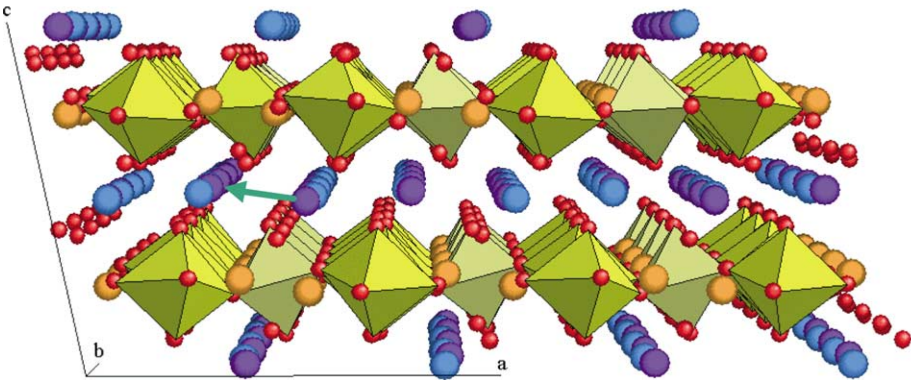

Fig. 1. Crystallographic structure of monoclinic zirconolite. Ca, Zr and O atoms are in blue, purple and red respectively. The TiO_6 ocathedra are indicated in yellow and green as well as the five-fold coordinated Ti atoms in orange. The green arrow indicates the direction of the observed RCS (see text).

Table 1
Fitted parameters of the short-range rigid-ion Buckingham potentials for $CaZrTi_2O_7$

Interaction	A (eV)	ρ (Å)	C (eV Å^6)
O^{2-}–O^{2-}	*22 764*	*0.1490*	32.8
Ca^{2+}–O^{2-}	1412	0.3382	*0*
Zr^{4+}–O^{2-}	1937	0.3440	*0*
Ti^{4+}–O^{2-}	942	0.3479	*0*
U^{4+}–O [51]	*895.6*	*0.42512*	*65.4*

Figures in italics were kept constant during the fit.

Table 2
Comparison between experimental and calculated crystallographic data, specific heat C_p and bulk modulus for zirconolite

Physical properties	Experimental	Calculated (present work)	Variation (%)
Lattice volume (Å^3)	1014.06 [19]	1015.71	0.16
Density (g/cm^3)	4.4418 [19]	4.4346	−0.16
a (Å)	12.4458 [19]	12.9161	3.78
b (Å)	7.2734 [19]	7.1100	−2.25
c (Å)	11.3942 [19]	11.3233	−0.68
β (°)	100.533 [19]	102.3721	1.83
C_p (J/g K) at $T = 295$ K	0.55 [52]	0.55	0.0
	0.62 [53]		11.3
Bulk modulus (GPa)		224.3	

3. Threshold displacement energies

3.1. Methodology and results

One of the most important parameters affecting radiation damage in a material is the threshold displacement energy (E_d) which is the minimum kinetic energy necessary to displace an atom from its equilibrium crystallographic site, entailing the formation of a stable close Frenkel pair. This parameter is fundamental for controlling the production of radiation damage in materials and as such, is useful to understand and model the effects of radiation on materials. MD simulation has the great advantage that it allows the realistic treatment of the atomic motions and naturally include the crystal structure effects. It is therefore possible with this method to calculate the threshold displacement energies needed as an input parameter for more macroscopic models such as the binary collision models (e.g. SRIM [16]). Since ceramics generally consist of multiple sublattices, E_d must be separately measured (or calculated) for each sublattice. However, E_d measurements, especially when one wishes to distinguish between the different types of atoms, are quite difficult. Some E_d values, experimental or calculated by computer simulations, are listed elsewhere for oxides [4,23,24]. But, to our knowledge, no values of the threshold displacement energies exist for the ceramic materials under consideration as matrices for radionuclides immobilization, except in the case of zircon ($ZrSiO_4$). For this material, experimental estimates [25] exist and calculated values for the different sublattices are available in literature [9,25,26].

In MD simulations, E_d can be easily calculated, for each ion type, by giving, in various directions, a series of impulsions of increasing kinetic energy to an atom of the chosen type, the primary knocked-on atom (PKA), and following the subsequent atomic motions. In each direction, for low energies, after some atomic displacements, the PKA and all the other displaced atoms readily return to their original positions, leaving the crystal unperturbed. Beyond a certain energy the PKA does not return to its original site. In this case, at least one (sometimes more) Frenkel pair remains at the end of the simulation. In this last case a small DC results from the impulsion initially given at the PKA. The E_d of the given ion type is then the minimum among the various directions of these threshold energies. We considered that E_d is reached when the PKA has left its original position by more than its first neighbor shell distance and for at least a simulated time of 0.3 ps. In these cases the Frenkel defect has reached an energetically *metastable* configuration (i.e. subsequent recombinations of the vacancy–interstitial pair remains possible by a thermally activated diffusion process).

We used a box containing 5632 atoms initially at 0 K. To save calculation time, we restricted the research of the threshold energies to a few crystallographic directions that we presumed to correspond to the lowest E_d values. We chose the directions oriented towards the dense (low index) ionic rows, the centers of the edges and the faces of the coordination polyhedra. The minimum for each ion type of the threshold energies over the crystallographic directions are reported in Table 3. They range between 15 for oxygen and 48 eV for zirconium. The E_d values are quite different among the different types. In particular, calcium and oxygen ions have a lower E_d. It is also worth noting that the E_d of the cations are larger than the oxygen one.

3.2. Discussion

Very different threshold displacement energies are found for the various types of atoms in zirconolite. The assumption that is sometimes done in binary collision

Table 3
Calculated threshold displacement energies (E_d)

Ionic site	E_d (eV) in zirconolite	E_d observed in literature for different oxides [9,23,32,33]
Ca	25	–
Zr	48	$41 \leqslant E_d \leqslant 97$
Ti	43	–
O	15	$20 \leqslant E_d \leqslant 70$

model that all E_d values are equal in a given compound is therefore wrong in the present case. The observed difference comes from the differences in ionic mass, charge and first neighbor shell. More precisely the smaller value observed for oxygen may come from the fact that the cations are encapsulated in their oxygen first neighbors shell. The destruction of this shell (needed for creating a cation Frenkel pair) costs a lot in energy. Such different values of E_d will result in nonstoichiometric damage production during high energy DCs (see below). This should also be the case for displacement indirectly induced by inelastic collision (electronic losses) of the recoil nucleus or the α particle created by the α disintegration.

As far as we know, there are neither experimental nor theoretical reliable E_d values yet available for zirconolite. Only averaged estimations exist, ranking from 15 to 40 eV [27–30]. Our values are in this range. Moreover they appear reasonable when compared to the most commonly observed range in ceramics, i.e. between 20 and 90 eV [31]. More precise comparisons are not possible for calcium and titanium atoms as no value exists for these ions in oxides. $E_d(\mathrm{Zr})$ and $E_d(\mathrm{O})$ have been experimentally [23,32] or computationally [9,26,33] estimated in different ceramics (Table 3). Our calculated values are compatible with these estimations. But they are lower than the ones obtained by Crocombette and Galeb [9] for zircon ($E_d(\mathrm{Zr}) = 90$ eV and $E_d(\mathrm{O}) = 32$ eV) which have been computationally determined using very similar potentials and following the same procedure as ours. This highlights the dependence of E_d with the atomic structure of the material.

An unexpected behavior appeared during the MD calculations of E_d. Indeed we sometimes observed replacement collision sequences (RCS) along specific low index crystallographic directions. Such RCS occur only for the Ca atoms accelerated along the [−1 1 0]-type (or equivalent) direction. The small DC produces series of replacement of Ca atoms along the [−1 1 0] direction and results in the formation of a vacancy and an interstitial a few interatomic distances away from each other. In such pure Ca rows, the atoms are perfectly aligned for temperatures near 0 K.

4. Displacement cascade simulations

4.1. Methodology

Due to computer limitations we were bound to compute very few cascades. With such a small number of events reproduced it is not possible to produce reliable statistics. Still we believe that the qualitative pictures obtained are of high interest and that the quantitative figures extracted from the calculations give some insight about the behavior of the material.

One uranium U^{4+} ion was incorporated and accelerated in zirconolite to simulate cascades initiated by heavy particles, thus modeling the effect of the α-decay recoil nucleus. The parameters of the U^{4+}–O^{2-} short-range potentials used in Eq. (1) are taken from reference [34]. The connection with Ziegler potential is made between 1.1 and 1.3 Å. The simulations were performed according to the following procedure. At first, a box containing many unit cells is built according to the regular fitted ionic positions and lattice parameters and one uranium U^{4+} ion is substituted for a zirconium Zr^{4+} ion. The structure is quenched to 0 K to reach the ground state. Before starting the collision cascades, the system is thermalized at room temperature during 3 ps. In the NVE ensemble (constant volume, energy and number of particles) this is achieved simply by initializing atomic velocities with a random Maxwellian distribution centered on 600 K. In a few tenth of picoseconds the temperature decreases to 300 K thanks to the equipartition of the energy between its kinetic and potential components.

Table 4
Characteristics of the DCs

Uranium energy (keV)	2	4	6	12
Uranium trajectory length (nm)	3.1	4.3	5.6	5.8
Maximal temperature (K)	445	589	734	1167
Simulated time (ps)	5.3	10.2	13.7	18.9
Number of displaced atoms (>0.8 Å)				
Ca	8	22	49	53
Zr	2	13	34	44
Ti	46	114	148	237
O	371	675	1025	1771
Total	428	825	1257	2106
Total number of defects	288	605	862	1310
Stored energy (eV)	49	111	204	334
Stored energy per defect (eV/at.)	0.17	0.18	0.24	0.25

An impulsion is then given to the uranium atom and the subsequent movements of the atoms inside the simulation box are followed until a metastable state is reached (i.e. picoseconds for the time scales of our simulations). Primary impulsions corresponding to kinetic energies from 2 to 12 keV have been considered (see below). These energies are smaller than expected in real waste containing materials where they would lie around 70 keV but they correspond to the maximum that we can tackle with our computer resources. During all the simulation, the temperature of a 0.3 nm wide external layer is kept constant at 300 K to model the thermal bath constituted in reality by the outer part of the crystal. For this purpose, the velocities of the atoms in the outer layer are regularly rescaled to maintain the kinetic energy calculated as an average on all atoms in the layer at a constant value of 300 K.

At the primary stage of a DC the velocities of the ions can reach quite high values. It is therefore necessary to use a time step as short as 10^{-5} ps to discretize the trajectories of the ions. After some 10^{-3} ps, the maximum atomic velocity decreases and the time step of the simulation can be increased. This is accomplished routinely by adjusting the time step so that the maximum atomic displacement between two consecutive time steps is smaller than 0.02 Å. Starting from 10^{-5} ps it slowly rises to 10^{-3} ps. The global temperature rises up to 1000 K during the unfolding of the DC. This maximum temperature is reached in less than one tenth of a picosecond. Then temperature gently decreases during the rest of the simulation down to values close to the fixed external layer value. The simulation is ended when the temperature gets down to 320 K. In order to perform some analysis on the atomic positions at the end of the cascade, the box is then quenched, using a fast quenching algorithm.

The cascades simulations were performed in a 1234 nm^3 box containing 106 920 atoms ($9 \times 15 \times 9$ unit cells). The initial trajectory of the PKA was oriented to a high index direction to avoid possible channeling. Four different primary kinetic energies have been considered (2, 4, 6 and 12 keV). Moreover, in order to assess the effect of cascades overlap, a second 12 keV DC was simulated after the first 12 keV cascade (see below).

4.2. Results

4.2.1. Displacement cascade unfolding

The characteristics of the cascades are reported in Table 4. The Figs. 2–6 relates to the 12 keV cascade that we chose to exemplify the behaviors common to all simulated cascades. In Figs. 3–5 a portion of the simulation box is shown. The directions are the same than in Fig. 1. At the beginning of the cascades ($t < 1$ ps), the uranium projectile provokes atomic displacements removing the atomic-scale periodicity. After 0.3 ps the projectile stops, but at that time the ballistic phase of the DC is still under progress. After about 1 ps the ballistic phase ends and a partial recovery occurs. The number of displaced atoms decreases and many of them return to their original crystallographic positions. The process of atomic displacement and partial recovery can be exemplified by monitoring the number of atoms displaced from their original crystal sites as a function of time

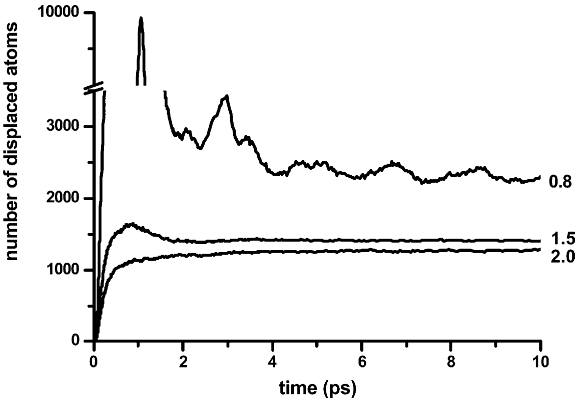

Fig. 2. Number of displaced atoms as a function of simulated time in the 12 keV DC. The upper, medium and lower curves are for cutoff distances of 0.8, 1.5 and 2.0 Å, respectively.

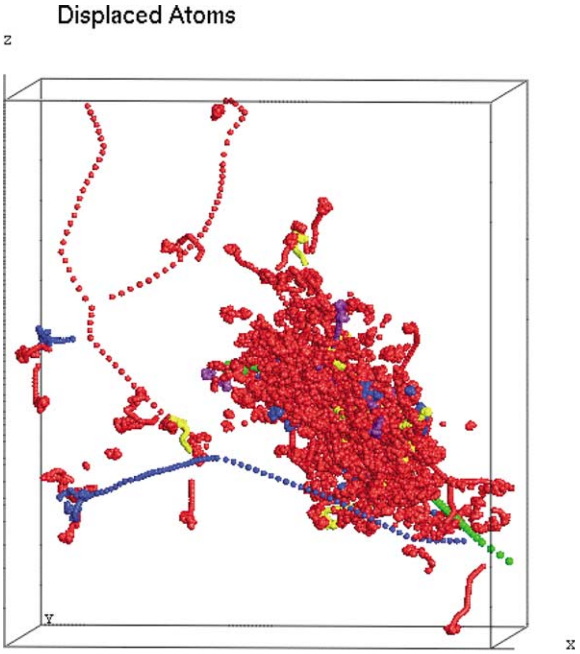

Fig. 3. Successive positions of atoms displaced by more than 4.0 Å in the 12 keV DC. Ca, Zr, Ti, O and U atoms are indicated in blue, purple, yellow, red and green, respectively. One can clearly see the subcascade initiated by the 4 keV calcium hit by the uranium at the beginning of its trajectory.

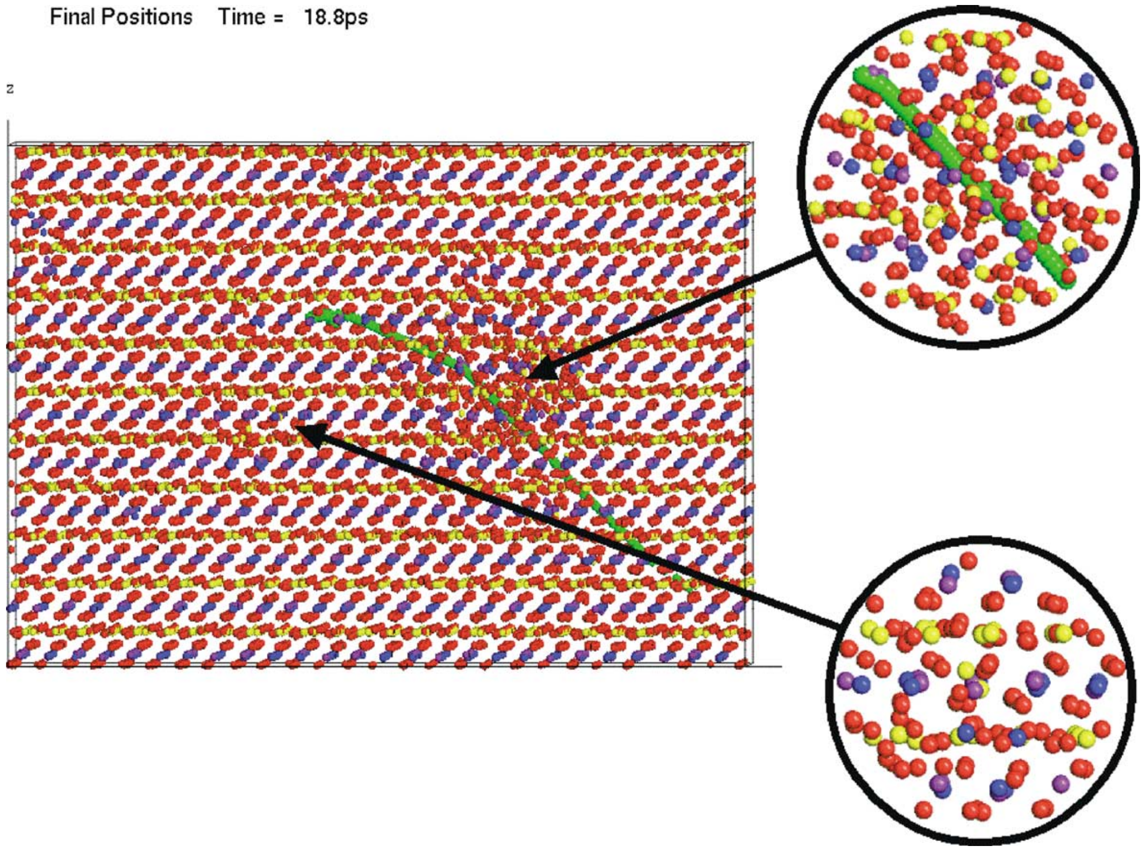

Fig. 4. Final configuration of the atoms at the end of the 12 keV cascade (i.e. after a simulated time of 18 ps). Ca, Zr, Ti, O and U atoms are indicated in blue, purple, yellow and red, respectively. The green spheres show the successive positions of the uranium during the cascade. The upper zoom shows a part of the disordered zone near the uranium track (10 Å radius sphere). The lower zoom exhibits some point defects disconnected from the track: a titanium dumbell in a Ca–Zr row and two Ca in a Ti row (7.5 Å radius sphere).

(Fig. 2). In the second picosecond after the beginning of the cascade, around 75% of the atoms displaced by more than 0.8 Å return to their original position. By the end of the simulation, when temperature has decreased to 320 K, the recovery process has ended and no further evolution can be seen at this timescale. Considering a larger cutoff distance one can conversely see that only 20% of the atoms displaced by more than 1.5 Å and none of those displaced by more than 2 Å return to their starting point during the simulation time (see Fig. 2). Some RCS inside calcium rows, very much like the ones we obtained during threshold displacement energies determination, were observed on the border of the cascade zone showing that such RCS are not specific to zero starting temperature. For the high primary kinetic energy (12 keV) a branching of the cascade in subcascades occurred. The uranium atoms transferred 4 keV to a calcium atom that initiates a separate cascade in another area than the uranium atom. This is clearly evidenced by Fig. 3 which is built from the positions of atoms displaced by more than 0.8 Å from their original sites. Once an atom has been classified as displaced, all its subsequent positions (calculated every 0.1 ps) are displayed in Fig. 3. One can clearly see the trajectory of the uranium atom (in green) as well as the ones of the calcium and oxygen secondary projectiles.

During the recovery process, we observed atomic displacements in titanium planes: some oxygen and titanium atoms are shifted inside titanium planes.

4.2.2. Structure of the cascade track

Fig. 4 shows the structure of the material after the final quenching of the 12 keV cascade. Eye inspection indicates that the maximum perturbation accumulates around the uranium track (in green) and especially in the second half of its trajectory. In this area the crystalline order is highly perturbed and qualitatively one could say that it is essentially lost (see below for a quantitative analysis). But one can learn from Fig. 3 that many displaced atoms are situated quite far away from this central track. In these regions little perturbation can be seen by eye inspection in the global picture of Fig. 4.

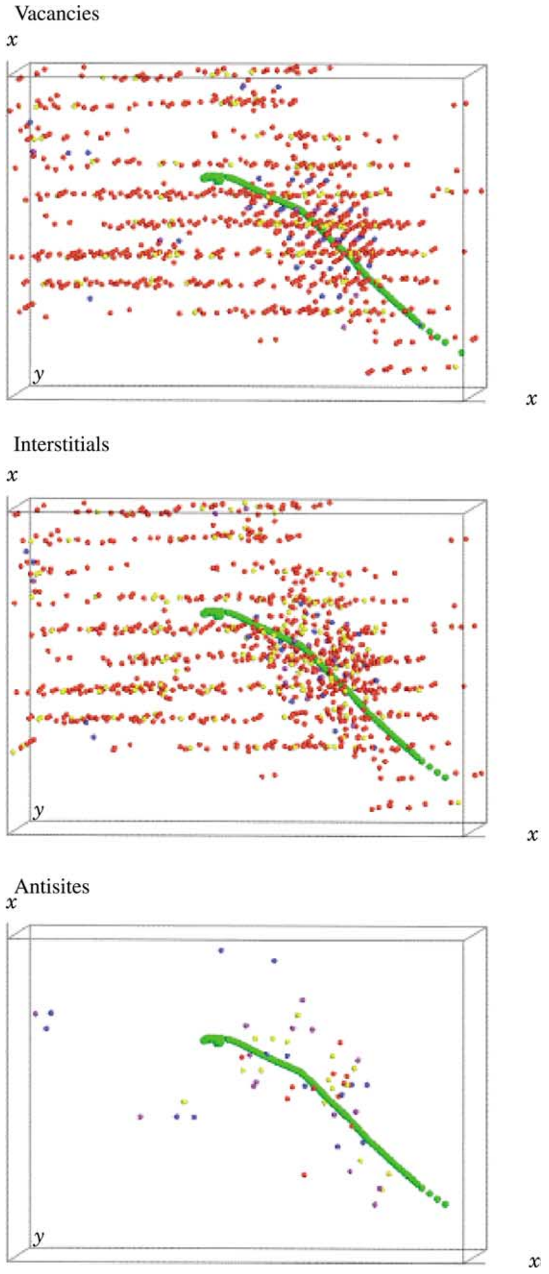

Fig. 5. Defects produced by the 12 keV DC, from top to bottom: vacancies, interstitials and antisites. Ca, Zr, Ti and O atoms are indicated in blue, purple, yellow and red, respectively. The green spheres show the successive positions of the uranium during the cascade. One can clearly observe the central area of high disorder and the point defects disconnected from it.

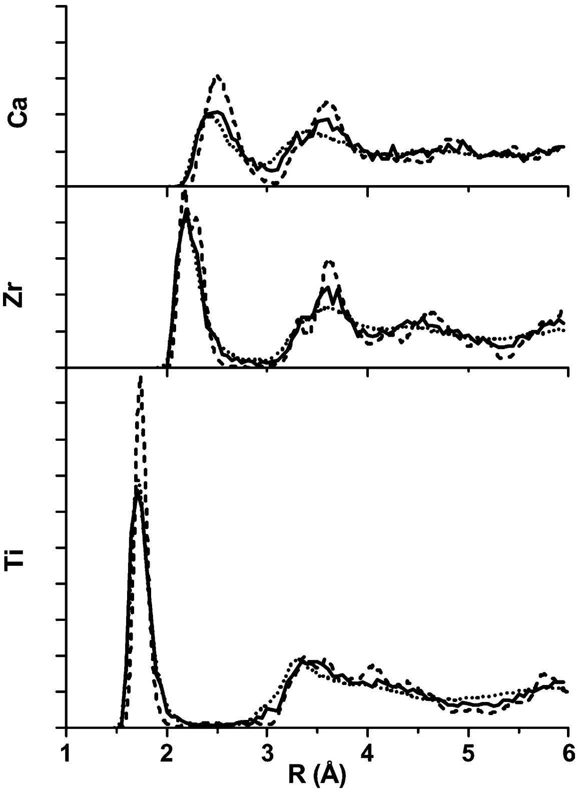

Fig. 6. RDF around the cations at room temperature. The solid line is characteristic of the core of the cascade track (see text). Dashed and dotted lines are for the crystalline and amorphous materials, respectively.

However having experienced atomic displacements these areas also include disorder, as it can be seen from the lower zoom in Fig. 4. Indeed they contain many point defects: vacancies (empty site), interstitials (atom not situated in any crystalline site) or inequivalent substitutions i.e. antisite inversions (e.g. a calcium atom ending in a zirconium site). To precisely count these point defects we used the following criteria: for each site in the perfect crystal, one considers a sphere of radius 0.8 Å around this site. If this sphere is empty the site is classified as a vacancy; if it is occupied by an atom of a different kind than before the cascade a substitution is obtained. It can also happen that the sphere is occupied by a different atom than before the cascade but of the same type. We shall then speak of replacements which are not point defects. With the chosen radius no double occupancy ever occurred. Finally, the atoms that are not contained in any sphere are classified as interstitials.

Pictures of the different kind of defects are given in Fig. 5. Many point defects appear far away from the main track. Some are isolated and some are gathered in small clusters especially at the end of the trajectories of the subcascade projectile. The density of defects in the central area is very large. It appears difficult to speak in term of point defects within a crystalline material. We would rather qualify the central area as highly disordered (see below). As the core of the cascade track does not remain crystalline, the number of point defects as given in Table 4 is of little signification. Indeed, with our brute force definition of point defects, a completely amorphous material would contain as many defects as atoms. In order to quantify the amount and the nature of the disorder inside the uranium track, we calculated the radial distribution function (RDF) of the atoms inside a small sphere (radius $= 15$ Å) centered on the track. This radius was chosen empirically to obtain the largest possible sphere inside the ellipsoid made by the track. The RDF has been calculated on the atomic configuration obtained at the end of the cascade simulation before the final quenching. The RDF therefore includes the contribution of thermal disorder. We compared it to the RDF of crystalline and amorphous material at room temperature. To built the amorphous RDF, we heated up the 106 920 atom box to 24 000 K and cooled it down to room temperature. We used the smallest possible cooling rate with our computers, i.e. 10^{15} K/s. This cooling rate is in fact extremely large and it is possible that the final amorphous structure is not correct due to this too fast quenching.

The complete RDF of the cations are plotted in Fig. 6. One can see that the first peak (due to oxygen first neighbors) is very similar in the amorphous material and in the cascade core. They are much broader than in the crystal indicating an higher disorder. A very slight shifting of the maximum of the first peak towards smaller distances is also visible. The number of oxygen first neighbors around the cations have been calculated by integration of their specific (cation–oxygen) RDF. Titanium and zirconium ions keep the same number of neighbors in the different samples. Calcium atoms have fewer neighbors in the amorphous material and in the cascade core (a bit less than seven neighbors) than in the crystal (eight neighbors). Subsequent peaks after 3.0 Å are visible in the RDF of the crystalline material. The main contribution to these peaks are the second neighbors cation–cation pairs. The amorphous RDF are much more blurred and exhibit only very broad, structure-less, peaks. At the opposite of what was observed for the first peak, the RDF of the cascade core is quite close to the ones of the crystal.

A second 12 keV cascade have been introduced in the box at the end of the first 12 keV cascade simulation. The projectile was directed approximately towards the first track. The main feature of the second cascade is that the disorder in the zone of tracks recovering, as measured with the RDF and point defects, is the same after one or two cascades.

4.2.3. Variation of the behavior with the projectile energy

Beyond the common behaviors described above, some differences appear when one considers the various kinetic energies of the uranium projectile. The number of atomic displacements and defects varies linearly with the projectile energy (see Fig. 7). The main irregularity that shows up for the 12 keV cascade may be due to the appearance of subcascades that we observed only for this energy. One could also note that the smaller the energy of the projectile is, the better the recrystallization takes place in the track. Indeed for large energies the recrystallization only takes place in the peripheral zone of the track leaving an amorphous core, whereas the 2 keV cascade exhibits a nearly complete recrystallization in the whole cascade volume. We calculated the energy stored during the DCs by comparing the potential energies of the boxes at 0 K before and after the cascade. One could see (Table 4 and Fig. 7) that only 3% of energy inserted into the system is eventually stored by it, most of the kinetic energy being pumped away by the external thermal bath. The variation of the stored energy with the projectile impulsion shows a logical rising trend almost linear even if an irregularity appears between 4 and 6 keV.

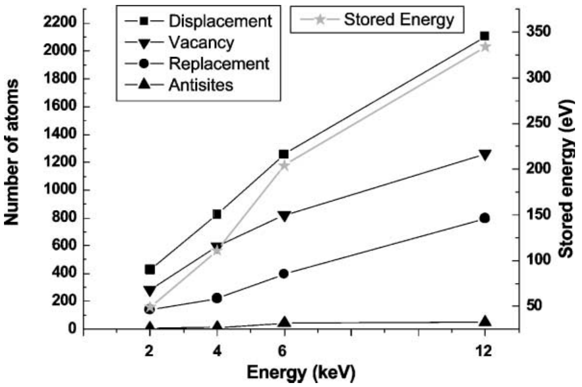

Fig. 7. Variation of the number of defects and stored energy with the projectile energy.

5. Discussion

5.1. Nature of the defects created by the cascade

Our calculations show that a recoil nucleus cascade in zirconolite result in different kinds of defects. First, the central area around the projectile track is highly disordered during the cascade and ends in a quasi-amorphous state. Second, point defects are spread around the track. These point defects can be clearly identified as isolated interstitials, vacancies or antisite defects and some are situated quite far away from the track and are thus clearly disconnected from it.

This complex picture can be explained in view of the fast dynamical reconstruction that occurs after the initial ballistic stage of the cascade. This reconstruction process is strong enough in peripheral zones, far away from the uranium track, to rebuilt the crystal leaving only point defects. In the central area the reconstruction also takes place. For low projectile energies (2 keV) the induced disorder is small enough to make the recovery of the crystal nearly as complete in the track as it is in the periphery of it. The track in this case appears only as a rough cylinder of high density of point defects. For higher energies, the size of the perturbed area and the amount of disorder are large enough so that the reconstruction process is only partial. We observed that in these cases the reconstruction proceeds dynamically from the outer crystalline to disordered area. This indicates that the reconstruction acts by an epitaxial process. This phenomenon is commonly observed in materials under irradiation effects [35]. The irregularity observed in the rise of the stored energy with the projectile initial impulsion that we observed between 4 and 6 keV may be due to the persistence of a disordered area for the higher energies. Such an area may store less energy than a point defects zone.

5.2. Comparison with experiment

In spite of many experimental studies (see [4,5] for reviews) little experimental facts can be directly compared to our results. We discuss results of EXAFS studies and measurements of the energy stored during amorphization.

Some EXAFS studies of partly or completely amorphized zirconolite have been performed [36–40]. The findings differ between these studies, but there seems to be a consensus on the following facts comparing the amorphous phase to the crystalline one at the atomic scale:

- a distortion appears for the first coordination shell of cations;
- in this shell the lengths of the bonds are reduced and the number of neighbors tends to decrease especially for Ti and Ca;
- the second neighbors distances tend to be larger;
- there is a general loss of order after the first shell that may be due to the rotation of the polyhedra around common vertices or summits.

Our results compare partly with these experiments. Indeed, in our calculations for the amorphous phase, a distortion appears for the first shell of the cations, the corresponding oxygen distances are a little smaller than in the crystal and the order is essentially lost beyond first neighbors. The decrease in the first coordination shell is only observed for calcium ions and we did not observe any increase of second neighbor distances. Our model of the amorphous phase is therefore not perfect but the main trends of the differences between the crystal and amorphous phases are reproduced. The analysis of the disordered tracks showed that they are not fully amorphous. Indeed their RDF beyond the first peak, typical of the cation–cation ordering, exhibit higher order than in the simulated amorphous material. This distinction may be real. Indeed, Clinard et al. [41] observe different metamict states (i.e. disordered under irradiation) depending on the irradiation conditions. But it may also come from the low energy of our projectile or from a bad description of the amorphous materials due either to the too fast quenching or to the weaknesses of the empirical potentials.

The stored energy at complete amorphization has been measured in natural [42,43], Cm doped zirconolite [44,45] and the pyrochlore $CaPuTi_2O_7$ [43,46]. It lies between 34 and 48 J/g which corresponds to 0.11–0.16 eV/at. Upon irradiation accumulation, the stored energy goes through a maximum between 100 (0.33 eV/at.) and 200 J/g (0.70 eV/at.) [43,46]. It then decreases before complete amorphization. This has been analyzed in terms of cascade recovering which could induce partial annealing. To compare our values of the energy stored during one cascade with experimental figure we have to define a number of atoms ‘perturbed’ by the cascade to divide our global value and obtain a stored energy per atom. Dividing the stored energy by the number of defects at the end of the cascade (as defined before and plotted in Fig. 5) we obtain values of the stored energy per defective atom between 0.17 and 0.25 eV. These figures are in very good agreement with experimental values. It is however difficult to discuss further as our figures depend highly on the quite arbitrary definition of the number of perturbed atoms.

5.3. Comparison with other materials and macroscopic behavior

The effects of α recoil nucleus irradiation in zirconolite are quite different from what is observed in other crystalline oxides studied in the same theoretical framework. Previous MD using very similar BMH empirical potentials were performed on zircon [9] and uranium dioxide [47]. In zircon recoil nucleus only creates an amorphous core around the track with no surrounding point defects. At the opposite in urania the simulation ends with a collection of vacancies and interstitials widespread in the material with no specific defects around the path of the projectile. The effect of an heavy projectile in zirconolite thus seems to be intermediate the one in zircon and urania.

The differences in single particle effects between zircon and urania have consequences on the global and cumulative effects of irradiation in these materials. Indeed zircon undergoes under irradiation a transition from a crystalline to an amorphous state. This transition is of the direct impact type, i.e. each projectile directly produces an amorphous zone [48]. At the opposite urania cannot be amorphized under irradiation [49]. In these two cases there is a direct correspondence between single particle and global irradiation effects. We should note however that some compounds are amorphized by a point defects accumulation effect, so the fact that recoil nucleus produces only point defects in urania is coherent with the observed absence of amorphization but does not imply it.

Not surprisingly, the behavior of zirconolite is a bit more complex. Under α-decay accumulation or external ion irradiation, zirconolite is known to become metamict. Based on electronic and X-ray diffraction studies and swelling analysis, the amorphization is thought to be of the direct impact type (see [4] and references therein). However zirconolite does not simply go from crystalline to amorphous under irradiation. In the same time, a phase transition occurs in what remains of the crystalline materials. X-rays and electron diffraction studies [4] show that zirconolite goes from the monoclinic structure to a fluorite structure. An intermediate pyrochlore structure has also been recently observed between the monoclinic and fluorite structure [50]. These phase transitions are interpreted as the evidence that a part of the cascade energy is transferred to the crystallites and induces significant atomic rearrangements.

Our calculations are in agreement with the direct impact amorphization picture. Indeed we observe an metamict core around the track. The phase transitions of the crystalline material are not observed in our calculations. But the creation of point defects far from the central track is not incoherent with the observation of phase transitions in the crystalline zone. Point defects clearly evidence that some energy is transferred to the crystalline areas. They may also play a role in the observed phase transitions. First, point defects mechanically destabilize the monoclinic crystalline structure. It is possible that the pyrochlore and cubic structures are less destabilized than the monoclinic one so that they become energetically favorable at some point, for some amount of point defects for instance. Unfortunately the determination of phase stability at nonzero temperature in the presence of many defects is a very complicated task that goes far beyond the scope of the present study. Second, due to the inequivalent replacements during the cascade many antisites are created in the crystal. The accumulation of such antisites leads to a disordering of the cations and may favor the appearance of a fluorite disordered solid solution. Finally, point defects greatly enhance diffusion processes that may be important in the phase transitions.

6. Conclusion

We have established a rigid-ion force field for the modeling of the monoclinic zirconolite. An overall correct structure was obtained and the model presents satisfactory agreement with experimental density, specific heat and a correct order of magnitude for the bulk modulus. Using this force field, we have first evaluated the threshold displacement energies for the different ions by means of MD simulations. Very different values are found for the various ions. They are in the range of what is commonly observed in oxides.

MD simulations of displacements cascades have been carried out for energies between 2 and 12 keV. The results show that the zirconolite tends to a structural disordering around the projectile track for high PKA kinetic energy values. In the same time, point defects disconnected from the disordered zone are spread around the track. The epitaxial reconstruction phase is responsible for this complex behavior. These results are in agreement with the experimentally observed amorphization of the direct impact type. The phase transitions that occur in the crystalline phase are not reproduced by our calculations but the creation of many point defects is coherent with such phase transitions.

In the calculations zirconolite exhibits an intermediate behavior between direct amorphization (in the core track) observed in zircon ($ZrSiO_4$) and the point defect production observed in UO_2 by MD. These differences have a correspondence with the experimental differences between zircon (sole amorphization), zirconolite (amorphization and crystalline phase transitions) and urania (accumulation of point defects). This study, beyond the case of zirconolite, therefore shows that MD calculations using empirical potentials as crude as two-body BMH potentials are able to reproduce subtle differences in the behavior of ceramics under irradiation.

References

[1] G.R. Lumpkin, K.P. Hart, P.J. McGlinn, T.E. Payne, Radiochim. Acta 66&67 (1994) 469.

[2] K.L. Smith, N.J. Zaluzec, G.R. Lumpkin, J. Nucl. Mater. 250 (1997) 36.

[3] E.R. Vance, B.D. Begg, R.A. Day, C.J. Ball, Mater. Res. Soc. Symp. Proc. 353 (1995) 767.

[4] W.J. Weber, R.C. Ewing, C.R.A. Catlow, T. Diaz de la Rubia, L.W. Hobbs, C. Kinoshita, Hj. Matzke, A.T. Motta, M. Nastasi, E.K.H. Salje, E.R. Vance, S.J. Zinkle, J. Mater. Res. 13 (1998) 1434.

[5] R.C. Ewing, W.J. Weber, F.W. Clinards Jr., Prog. Nucl. Energ. 29 (1995) 63.

[6] D. Bacon, T. de-la-Rubia, J. Nucl. Mater. 216 (1994) 275.

[7] N.V. Doan, H. Tietze, Nucl. Instrum. and Meth. B 102 (1995) 58.

[8] J.M. Delaye, D. Ghaleb, Phys. Rev. B 61 (2000) 14481.

[9] J.P. Crocombette, D. Ghaleb, J. Nucl. Mater. 295 (2001) 167.

[10] B.G. Dick, A.W. Overhauser, Phys. Rev. 112 (1958) 90.

[11] J.D. Gale, Philos. Mag. B 73 (1996) 3.

[12] G.V. Lewis, C.R.A. Catlow, J. Phys. C 18 (1985) 1149.

[13] S.W. de Leeuw, J.W. Perram, E.R. Smith, Proc. Roy. Soc. Lond. A 373 (1980) 27.
[14] A. Abbas, J.M. Delaye, D. Ghaleb, G. Calas, J. Non-Cryst. Solids, in press.
[15] J.M. Delaye, D. Ghaleb, Mater. Res. Soc. Symp. 465 (1997) 633.
[16] J.F. Ziegler, J.P. Biersack, U. Littmark, The Stopping and Range of Ions in Solids, Pergamon, New York, 1985.
[17] L. Verlet, Phys. Rev. 159 (1967) 98.
[18] L. Veiller, J.P. Crocombette, C. Meis, D. Ghaleb, J. Phys. IV France 11 (2001) 251.
[19] H.J. Rossell, J. Solid State Chem. 99 (1992) 52.
[20] C.R.A. Catlow, Proc. Roy. Soc. Lond. A 353 (1977) 533.
[21] H. Özkan, L. Cartz, J.C. Jamieson, J. Appl. Phys. 45 (1974) 556.
[22] R.P. Ingel, D. Lewis, J. Am. Ceram. Soc. 71 (1988) 265.
[23] S.J. Zinkle, C. Kinoshita, J. Nucl. Mater. 251 (1997) 200.
[24] G.P. Pells, J. Nucl. Mater. 155–157 (1988) 67.
[25] R.E. Williford, B.D. Begg, W.J. Weber, N.J. Hess, J. Nucl. Mater. 278 (2000) 207.
[26] C. Meis, J. Nucl. Mater. 289 (2001) 1.
[27] K.D. Reeve, J.L. Woolfrey, J. Aust. Ceram. Soc. 16 (1980) 10.
[28] K.L. Smith, N.J. Zaluzec, G.R. Lumpkin, J. Nucl. Mater. 250 (1997) 36.
[29] L.M. Wang, S.X. Wang, J. Lian, R.C. Ewing, in: 1st Annual Michigan Materials Research Symposium, 1999.
[30] T.J. Headley, G.W. Arnold, C.J.M. Northrup, Mater. Res. Soc. Symp. Proc. 11 (1982) 379.
[31] L.W. Hobbs, F.W. Clinard Jr., S.J. Zinkle, R.C. Ewing, J. Nucl. Mater. 216 (1994) 291.
[32] R. Devanathan, W.J. Weber, L. Boatner, Mater. Res. Soc. Symp. Proc. 481 (1998) 419.
[33] R. Williford, R. Devanathan, W. Weber, Nucl. Instrum. and Meth. B 141 (1998) 94.
[34] R. Jackson, J. Huntington, R. Ball, Radiat. Eff. Def. Solids 134 (1995) 161.
[35] S.X. Wang, L.M. Wang, R.C. Ewing, Phys. Rev. B 63 (2000) 024105.
[36] R. Greegor, F. Lytle, R. Ewing, R. Haaker, in: K. Hogdson, B. Hedman, J. Penner-hahn (Eds.), EXAFS and Near-edge Structure III, vol. 2, Springer-Verlag, Berlin, 1984, p. 343.
[37] R. Greegor, F. Lytle, R. Ewing, R. Haaker, Nucl. Instrum. and Meth. B 1 (1984) 587.
[38] R. Greegor, F. Lytle, R. Livak, F.W. Clinard Jr., J. Nucl. Mater. 152 (1988) 270.
[39] F. Farges, Am. Mineral. 82 (1997) 44.
[40] F. Farges, R. Ewing, G.E. Brown Jr., J. Mater. Res. 8 (1993) 1983.
[41] F.W. Clinard Jr., D. Peterson, D. Rohr, L. Hobbs, J. Nucl. Mater. 126 (1984) 245.
[42] G.R. Lumpkin, R. Ewing, B. Chakoumakos, R. Greegor, F. Lytle, E. Foltyn, F.W. Clinard Jr., L. Boatner, M.M. Abraham, J. Mater. Res. 1 (1986) 564.
[43] F.W. Clinard Jr., E. Foltyn, R. Ewing, J. Nucl. Mater. 185 (1991) 202.
[44] W. Weber, J. Wald, Hj. Matzke, J. Nucl. Mater. 138 (1986) 196.
[45] W. Weber, J. Wald, Hj. Matzke, Mater. Res. Soc. Symp. Proc. 44 (1985) 679.
[46] E. Foltyn, F.W. Clinard Jr., J. Rankin, D. Peterson, J. Nucl. Mater. 136 (1985) 97.
[47] N.D. Morelon, D. Ghaleb, private communication.
[48] S. Rios, E.K.H. Salje, R.C. Ewing, J. Phys. Condens. Mat. 12 (2000) 2401.
[49] Hj. Matzke, J. Whitton, Can. J. Phys. 44 (1966) 995.
[50] S.X. Wang, L.M. Wang, R.C. Ewing, G.S. Was, G.R. Lumpkin, Nucl. Instrum. and Meth. B 148 (1999) 704.
[51] T. Karakasidis, P.J.D. Lindan, J. Phys. Condens. Mat. 6 (1994) 2965.
[52] W.J. Buykx, J. Nucl. Mater. 107 (1982) 78.
[53] B.F. Woodfield, J. Boerio, J.L. Shapiro, R.L. Putnam, A. Navrotsky, J. Chem. Thermodyn. 31 (1999) 245.